Phosphorus modified Ni-MOF–74/BiVO$_4$ S-scheme heterojunction for enhanced photocatalytic hydrogen evolution

Hongying Li, Haiming Gong, Zhiliang Jin [*]

School of Chemistry and Chemical Engineering, Ningxia Key Laboratory of Solar Chemical Conversion Technology, Key Laboratory for Chemical Engineering and Technology, State Ethnic Affairs Commission, North Minzu University, Yinchuan 750021, PR China

ABSTRACT

Regulating the directional migration of photo-generated carriers is an important strategy for realising high-performance photocatalysts. In this work, nano-particle Ni$_2$P and peanut-like BiVO$_4$ were grown on a rhombic structure Ni-MOF-74 substrate. A composite catalyst Ni-MOF-74/BiVO$_4$/P with excellent performance was prepared by the high-temperature calcination method. Phosphorus modification produces Ni$_2$P as an electron-capture centre while maintaining the basic morphology of Ni-MOF-74, effectively avoiding the accumulation of nanoparticles. The Ni$_2$P nanoparticles not only increase the number of active sites but also introduce negatively charged P that captures more protons for hydrogen evolution. After reasonable modification, the hydrogen production of the Ni-MOF-74/BiVO$_4$/P reached 245.4 µmol in 5 h, 23 times that of pure Ni-MOF-74. An S-scheme heterojunction between Ni-MOF-74 and BiVO$_4$ achieves the directional transfer of carriers thereby inhibiting the recombination of electron-hole pairs. The band structure and density of states of Ni$_2$P and BiVO$_4$ were determined in density functional calculations. This work provides a new way for the regulation of the carrier-behaviour in photocatalysts.

1. Introduction

Photocatalytic water splitting has received extensive attention from the scientific community as a new energy-production technology [1,2]. Most of the existing research has focussed on preparation of the photocatalyst, the core component of photocatalytic water splitting technology. At the beginning of this technology, the most of the catalysts with significant hydrogen production performance were prepared from precious metals [3,4]. However, besides being expensive, precious metal materials tend to produce metal residues during the reaction process, which are unfavourable to the environment [5]. To avoid these problems, the current research on photocatalytic water-splitting technology focusses on low-cost, non-toxic and efficient non-precious metal materials [6]. An efficient photocatalyst requires the correct morphology, size and dispersion, effective separation of electrons, and the effective use of sunlight [7]. However, a single catalyst has serious carrier recombination, low electron separation efficiency and a narrow range of visible light absorption capabilities, resulting in insufficient photocatalytic performance [8,9]. Hence, the preparation of catalyst with excellent catalytic performance is an important research strategy for photocatalytic water splitting technology.

Metal-organic frameworks (MOFs) are used as a new type of functional materials due to the diversity of their structures and functions. When used in heterojunction formation with other semiconductors they provide a platform that extends the life of the electrons involved in photocatalysis [10]. Meanwhile, MOFs with different morphologies such as zero-dimensional, hollow structures, one-dimensional tubes, two-dimensional sheets and three-dimensional arrays can used as a growth substrates for other semiconductor materials [11]. The derivative obtained from MOFs are known to possess strong good structures and high conductivity [12,13]. The derivatives of MOFs are generally obtained through decomposition at high temperature (between 500 °C and 900 °C). However, high-temperature thermal decomposition is accompanied by metal accumulation that can collapse the surface morphology of MOFs causing loss of its structural advantages [14–17]. Guo et al. found that Ni-MOF-74 exhibits a special thermal shock effect at 300 °C which effectively avoids the gathering of many metal particles [18]. Therefore, a metal-organic framework is a feasible option for obtaining the derivatives by thermal decomposition under lower temperature conditions. Ni$_2$P, which exhibits high catalytic activity due to its structural characteristics, can be obtained by phosphating Ni-MOF-74 at 300 °C. In recent years, transition metals with their metal-like

Table 1
Content of each component in the preparation of composite materials.

Sample	Ni-MOF-74 (mg)	BiVO$_4$ (mg)	NaH$_2$PO$_2$·H$_2$O (mg)
5-NBP	100	5	500
10-NBP	100	10	500
15-NBP	100	15	500
20-NBP	100	20	500
25-NBP	100	25	500
30-NBP	100	30	500

properties and good electrical conductivity have increasingly replaced precious metal materials as cocatalysts [19,20]. Phosphorous contained in transition metals has good electronegativity, drawing protons and facilitating the reduction of H$^+$ [21,22]. Hence, the use of Ni-MOF-74 as a support material in low-temperature phosphating and precursor material of Ni$_2$P an enticing prospect in photocatalysis research.

Bismuth vanadate (BiVO$_4$) includes three typical phases: a scheelite monoclinic phase, a scheelite tetragonal phase and a zircon tetragonal phase. Since its band gap (2.4 eV) can be excited by visible light [23–26], it can used to participate in photocatalytic reactions. Constructing a heterojunction with BiVO$_4$ and other materials can regulate the transfer behavior of carriers. These constructs overcome the poor adsorption capacity and migration of photo-generated electron-hole pairs in pure BiVO$_4$ [27]. Yu et al. proposed to construct an S-scheme heterojunction with two n-type semiconductors, one representing an oxidation catalyst, the other representing a reduction catalyst [28,29]. The S-scheme heterojunction avoids the low redox capacity of type-II heterojunctions and retains the useful electrons in the conduction band (CB) for the reaction. Therefore, an attempt was made to construct an S-scheme heterojunction to regulate the carrier transfer path and improve the photocatalytic performance.

In this work, the Ni-MOF-74/BiVO$_4$/P was prepared by combining the hydrothermal and calcination method. Ni-MOF-74 reduces the accumulation of large amounts of Ni$_2$P and BiVO$_4$ while taking full advantage of the high conductivity and metal-like properties of transition metal phosphides. Meanwhile, the S-scheme heterojunction provides an effective path for the transmission of electrons and efficiently separates the electrons. The study demonstrates the potential participation of MOFs as precursor materials in photocatalytic water splitting.

## 2. Experimental section

2.1. Synthesis of Ni-MOF-74

First, deionized water (20 mL), ethanol (20 mL) and dimethylformamide (DMF) (20 mL) were added to a 100 mL beaker and stirred for 10 min. Next, 1.6 g Ni(NO$_3$)$_2$ 6 H$_2$O, 0.48 g terephthalic acid and 2.4 g polyvinylpyrrolidone (K30) were added to the beaker and stirred vigorously for 30 min and then reacted for 10 h at 150 °C. Finally, the reaction solution was centrifuged and washed with ethanol and deionized water to obtain a light green substance, which was dried to obtain the final sample.

2.2. Synthesis of BiVO$_4$

Solution A was prepared by dissolving 3 mmol (0.3509 g) of NH$_4$VO$_3$ in 20 mL of deionized water with even stirring at 70 °C. Solution B was prepared by completely dissolving 3 mmol (1.4552 g) of Bi(NO$_3$)$_3$.5 H$_2$O in 30 mL of ethylene glycol. Solution A was added dropwise to solution B with stirring for 30 min, then reacted at 100 °C for 15 h in an autoclave.

2.3. Synthesis of Ni-MOF-74/BiVO$_4$/P

0.1 g Ni-MOF-74, 0.02 g BiVO$_4$ and 0.5 g NaH$_2$PO$_2$·H$_2$O were ground thoroughly, transferred to a porcelain boat and calcined in a tube furnace at 300 °C for 2 h. The whole process was carried out in a nitrogen atmosphere. The obtained sample (abbreviated as 20-NBP) was washed with deionized water and ethanol. The Ni-MOF-74/BiVO$_4$/P was changed by adjusting the dosage of BiVO$_4$. The specific component dosages are listed in Table 1. In addition, by adjusting the multiple of NaH$_2$PO$_2$·H$_2$O relative to Ni-MOF-74 (1, 3, 5, 7), the effect of phosphating degrees on the hydrogen evolution performance was explored without changing the amount of BiVO$_4$. The prepared samples were named 1–20-NBP, 3–20-NBP, 5–20-NBP and 7–20-NBP. In addition, the same calcination method is used to prepare Ni-MOF-74/BiVO$_4$, the difference is that NaH$_2$PO$_2$·H$_2$O is not added.
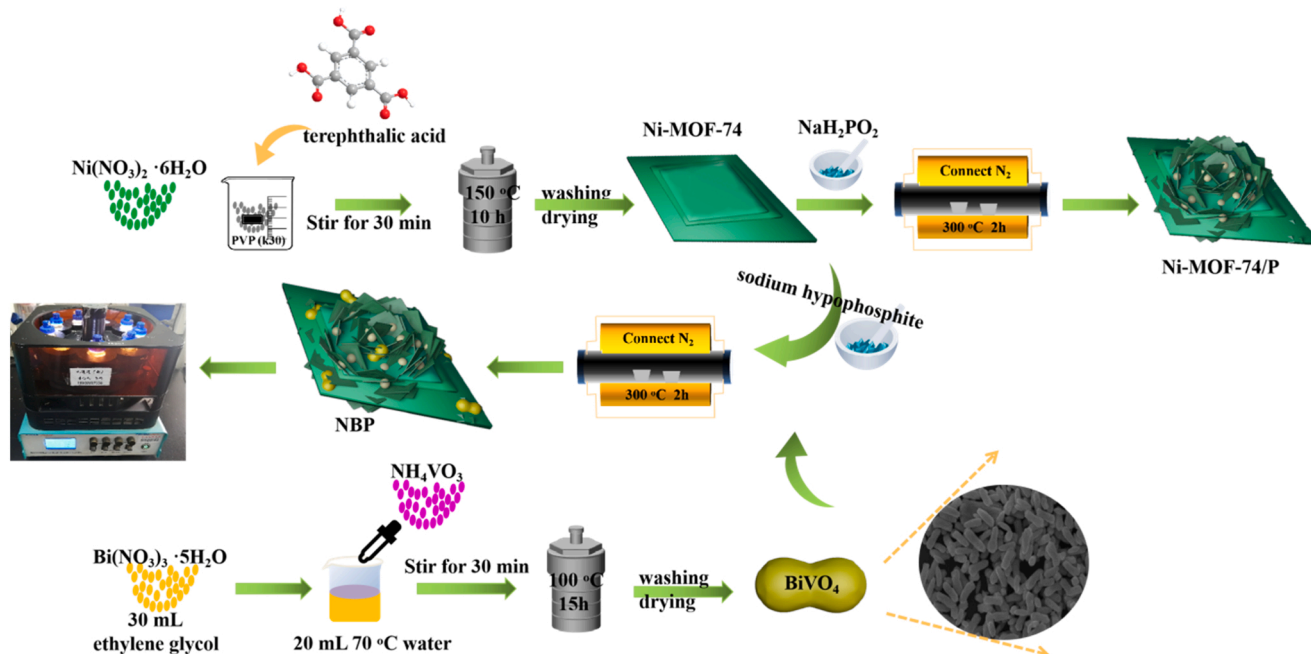
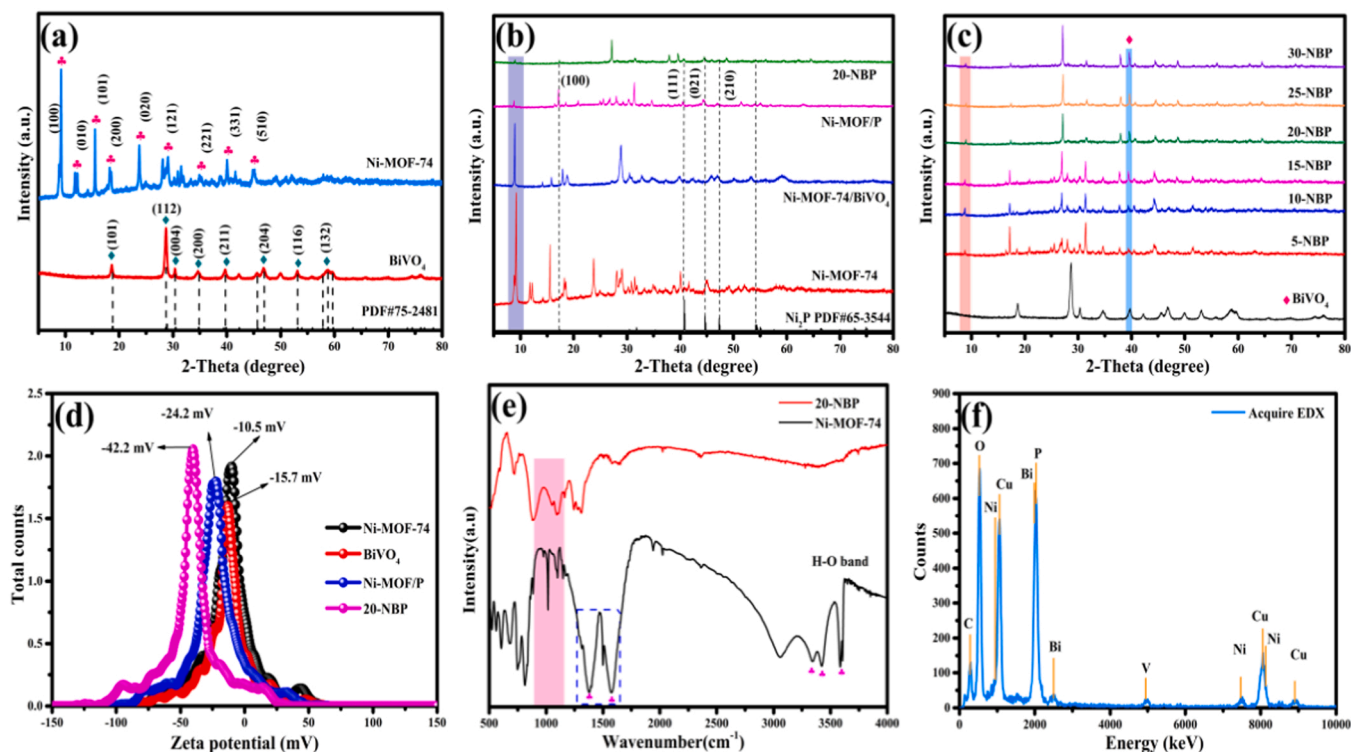**Scheme 1.** Synthesis processes of Ni-MOF-74/BiVO$_4$/P.

Fig. 1. XRD patterns of (a) Ni-MOF-74, BiVO$_4$; (b) Ni-MOF-74, Ni-MOF–74/BiVO$_4$, Ni-MOF/P and 20-NBP; (c) BiVO$_4$, x-NBP and (d) zeta potentials of the samples; (e) FT-IR spectra of Ni-MOF-74 and 20-NBP; (f) EDX pattern of 20-NBP.

2.4. Characterization

The morphologies of the materials were observed by a scanning electron microscope (SEM, JSM-6701F) and a transmission electron microscope (TEM, JEM1200EXJEOL) operated at 5.0 kV with a 300 kV acceleration voltage. The X-ray diffraction patterns of Ni-MOF-74, BiVO$_4$, Ni-MOF/P and Ni-MOF-74/BiVO$_4$/P were obtained using an X-ray diffractometer (XRD, Rigaku RINT- 2000, Cu Kα). The Fourier transform infrared spectra of the catalyst was measured at room temperature by a FTIR-650 Fourier transform infrared spectrometer. The surface valence states and element compositions of the samples were detected using X-ray photoelectron spectroscopy (XPS, ESCALAB 250Xi). The specific surface area of the catalyst was obtained by the Brunauer Emmett Teller (BET) equation on an ASAP 2020M instrument. The photoluminescence spectrum (PL) of the samples were acquired using a FluoroMAX-4 spectrometer (Horiba, France) at an excitation wavelength of 480 nm. The ultraviolet diffuse reflectance spectra against a BaSO$_4$ background were acquired by a UV-2550 (Shimadzu) spectrometer equipped with an integrating sphere.

2.5. Hydrogen evolution performance evaluation

The hydrogen production kinetics experiment of the samples were determined in a 62 mL quartz reaction flask under a 5 W LED lamp. First, 10 mg of the prepared photocatalyst and 20 mg of eosin Y (EY) were placed in the bottle, and 30 mL of triethanolamine solution (TEOA, 15% v/v, pH = 10) was added as a sacrificial reagent. Next, the solution was evenly dispersed using an ultrasonic cleaner. Finally, the air in the bottle was removed with nitrogen and bottle was placed in a multi-channel reaction system for the photocatalytic reaction at room temperature (25 °C). The amount of hydrogen produced was analysed by gas chromatography (Tianmei GC7900, TCD, 13Xcolumn, N$_2$ as carrier). For this purpose, 0.5 mL of gas was extracted from the reaction flask every hour.

2.6. Photoelectrochemical measurements

The samples were subjected to photoelectrochemical measurements on an electrochemical analyser (VersaStat4–400). Electrochemical test were performed in a standard three-electrode system with 0.2 mol/L Na$_2$SO$_4$ solutions solution and a 300 W Xenon lamp with a 420 nm filter as the light source. The three-electrode system included a platinum electrode, a saturated calomel electrode and a working electrode. The working electrode was prepared by mixing 5 mg of the catalyst with 10 μL of Nafion solution (10%). The mixture was sonicated into a uniform suspension for 30 min, then uniformly dropped onto an FTO glass sheet (1 × 2 cm^2) pretreated by washing with detergent (isopropanol, acetic acid solution, ethanol and water), covering an area of 1 × 1 cm^2 to form the working electrode. (Scheme 1).

2.7. Computational details

The band structure and density of states of Ni$_2$P and BiVO$_4$ were obtained by density functional theory. The cut-off energies in the calculations of Ni$_2$P and BiVO$_4$ were 400 eV and 520 eV respectively, and the energy convergence threshold of the self-consistent field was 1.00×10^{-5} eV. To optimise the structure, the convergence criteria were set to 0.05 eV/A (driving force) and 0.002 Å (maximum displacement). The exchange correlation potential was described by the Perdew-Burke-Ernzerhof (PBE) functional obtained with the generalized gradient approximation (GGA). Geometric optimisation and electronic-structure calculations were performed on Monkhorst-Pack grids composed of $4 \times 4 \times 1$ and $9 \times 9 \times 9$ k-points, respectively. In GGA-PBE calculation, the photoelectrons tend to delocalise due to self-interaction errors. To minimise this problem, the 3d orbitals of Ni and V were corrected using the DFT+U method.
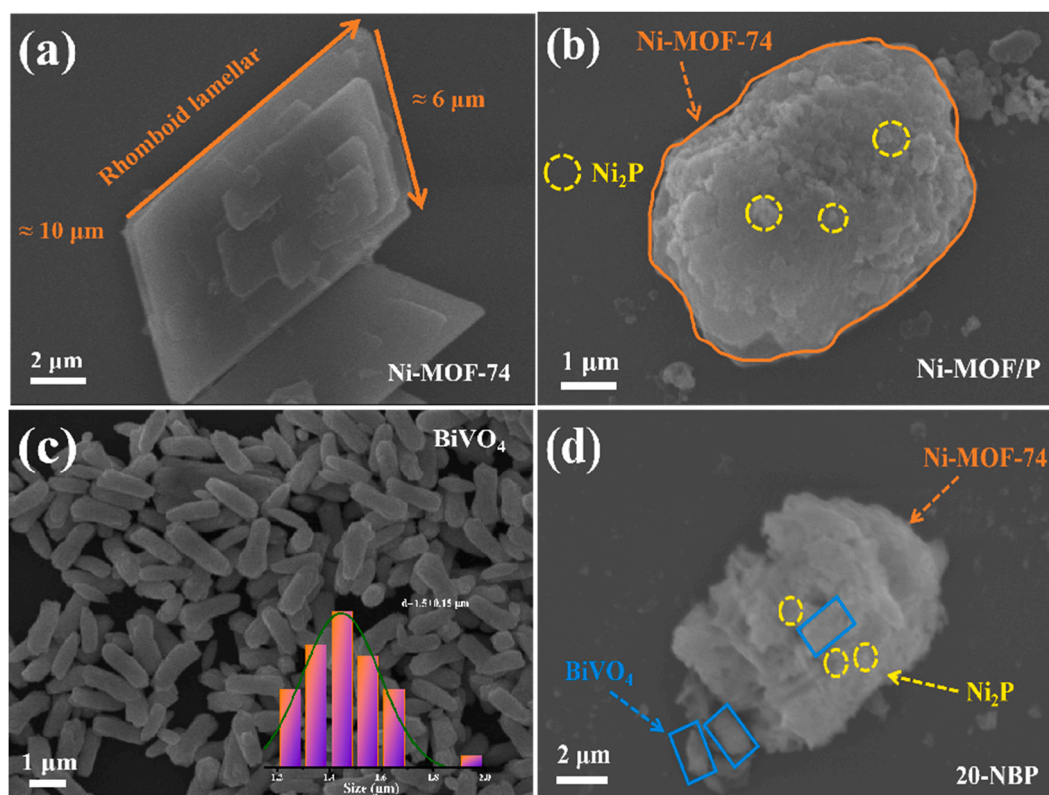
Fig. 2. SEM images of (a) Ni-MOF-74; (b) Ni-MOF/P; (c) BiVO$_4$ and (d) 20-NBP. The inset in (c) shows the size distribution of the bare BiVO$_4$ particles.

3. Results and discussion

3.1. Structure analysis

Fig. 1 shows the crystal phase structures of Ni-MOF-74, Ni-MOF/P, BiVO$_4$, Ni-MOF-74/BiVO$_4$ and x-NBP obtained by X-ray diffraction test (XRD). In the diffraction patterns of Ni-MOF-74 (Fig. 1(a)), the peaks at 2θ = 9.2°, 11.8°, 15.6°, 18.2°, 23.7°, 28.0°, 34.9°, 40.1° and 45.1° were well-matched to the (100), (010), (101), (200), (020), (121), (221), (331) and (510) crystal planes [30–32]. Peanut-like BiVO$_4$ also has good crystallinity and its diffraction peaks well corresponded with the standard card PDF#75-2481, indicating the successful preparation of BiVO$_4$. The diffraction peaks appearing at 18.7°, 28.7°, 30.3°, 34.7°, 39.8°, 46.9°, 53.1° and 58.7° were assigned to the (101), (112), (004), (200), (211), (204), (116)), (132) crystal planes of BiVO$_4$, respectively. In the diffraction pattern of Ni-MOF-74/BiVO$_4$, Ni-MOF/P and 20-NBP, the characteristic peak attributed to Ni-MOF-74 with reduced intensity can still be detected due to high temperature (Fig. 1(b)). In particular, the intensity of the diffraction peak at 9.2° belonging to Ni-MOF-74 was significantly weakened. The XRD pattern of Ni-MOF/P exhibited the peaks of both Ni-MOF-74 and Ni$_2$P. Compared with the diffraction peaks of the new peaks at 40.80°, 44.65°, 47.35° and 54.41°, not present in the spectrum of Ni-MOF-74, belonged to the (111), (021), (210) and (002) crystal planes of Ni$_2$P, respectively. The decisive presence of Ni$_2$P diffraction peaks indicates the successful preparation of transition metal phosphides. The coexistence of the diffraction peaks of Ni-MOF-74 and Ni$_2$P in Ni-MOF/P indicates that the metal organic framework is a feasible strategy as the support material and the precursor of Ni$_2$P. On the contrary, the peaks of Ni-MOF-74 and BiVO$_4$ were simultaneously detected in Ni-MOF-74/BiVO$_4$ without phosphating treatment. Therefore, high temperature and phosphating treatment are important factors that affect the intensity of the diffraction peak of the material. The relevant diffraction peaks of the internal non-phosphatised Ni-MOF-74 were enhanced because external phosphide has low crystallinity [33].

Fig. 1(c) shows the diffraction peak patterns of x-NBP with different BiVO$_4$ contents. Increasing the BiVO$_4$ content gradually enhanced the peak of the (211) crystal plane attributable to BiVO$_4$ further indicating the successful preparation of the composite material. The zeta potentials of the different materials are shown in Fig. 1(d). The zeta potential values of pure Ni-MOF-74 and BiVO$_4$ were − 10.5 mV and − 15.7 mV, respectively. After introducing Ni$_2$P to the original Ni-MOF-74 (forming Ni-MOF/P), the zeta potential significantly increased to − 24.2 mV, and the transition metal characteristic of Ni$_2$P enhanced the number of negative charges, proving that Ni$_2$P attracted carriers that participated in the reaction. The introduction of the Ni$_2$P and BiVO$_4$ in the composite concentrates the charge, resulting in a large zeta potential of − 42.2 mV. The highest negative charge was accumulated in 20-NBP intuitively signifying the greatly improved separation and transmission of internal electrons [34].

Fig. 1(e) shows the Fourier transform infrared (FT-IR) spectra of Ni-MOF-74 and 20-NBP, from which the chemical bonds and functional groups were detected. The vibration peak at 720 cm^{-1} in the spectrum of Ni-MOF-74 was caused by vibrations of the benzene ring substituted molecule above the plane vibration [35]. The bands at 1000–1100 cm^{-1} were assigned to C-H bending vibrations on the benzene ring [36], and those at 1580 cm^{-1} and 1379 cm^{-1} were the asymmetric and symmetric stretching vibrations of the coordinated carboxyl group, respectively [37,38]. As the entire test process was exposed to the atmosphere, the peak at 2362 cm^{-1} (C=O=C stretching vibration) in both materials was considered to be contributed by carbon dioxide in the air [39]. In addition, the stretching vibrations of water molecules in the 3346 cm^{-1} and 3429 cm^{-1} bands were attributed to coordinated water molecules in the Ni-MOF-74 [40]. No vibration bands of water molecules were detected in 20-NBP, implying that water molecules were lost by the high-temperature calcination treatment. EDX imaging (Fig. 1(f)) detected Ni, C, Bi, V, O, P and Cu elements in 20-NBP, confirming the preparation a high purity composite material. Among these elements, Cu element was selected as the detected element in the test process.
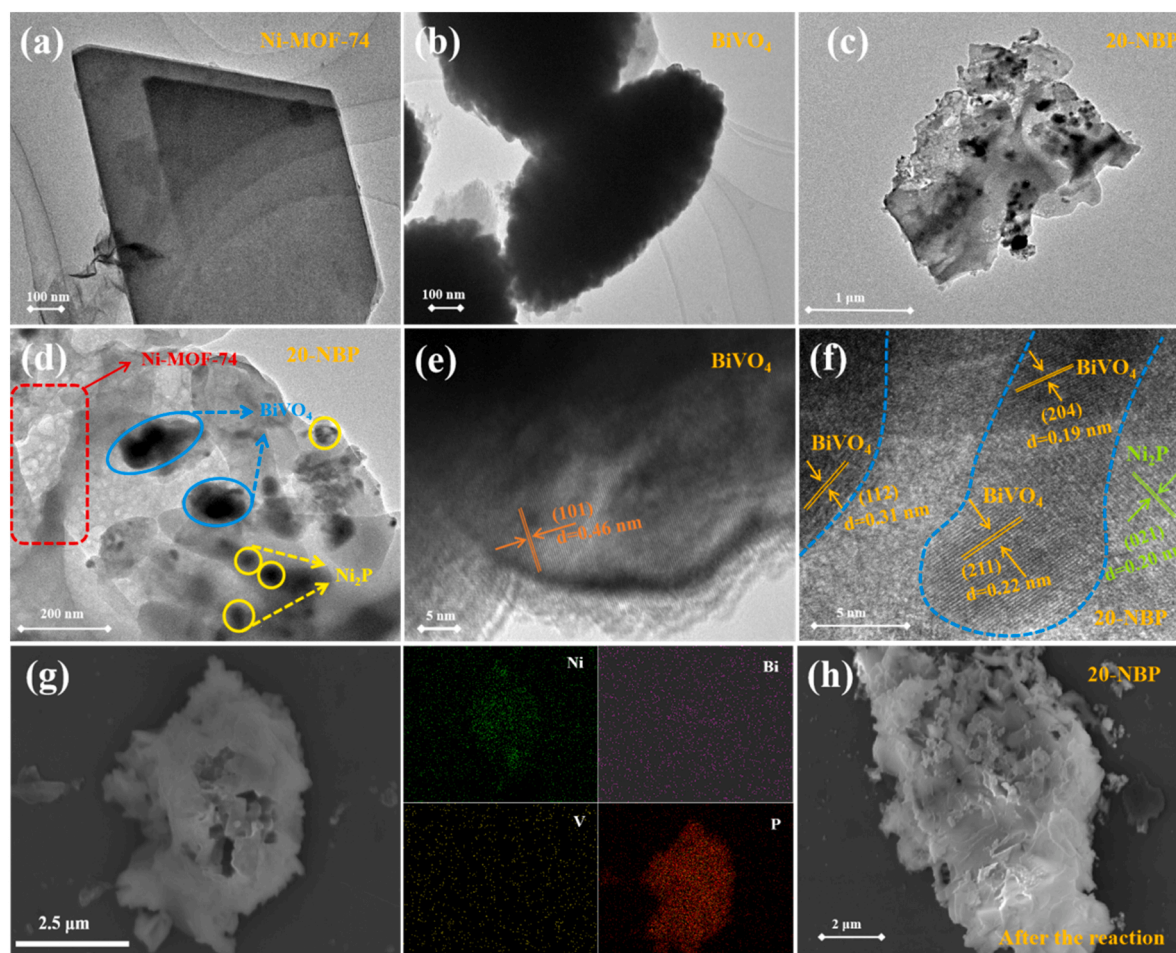
Fig. 3. TEM images of (a) Ni-MOF-74; (b) $BiVO_4$; (c,d) 20-NBP; HRTEM images of (e) $BiVO_4$; (f) 20-NBP; (g) elemental mapping of 20-NBP and (h) SEM image of 20-NBP after hydrogen production.

3.2. Morphological analysis

Fig. 2 shows the morphologies of Ni-MOF-74, Ni-MOF/P, $BiVO_4$ and 20-NBP. Single Ni-MOF-74 exhibited a smooth, regular rhombic structure with an approximate length and width of 10 μm and 6 μm, respectively (Fig. 2(a)). The rhombic surface of Ni-MOF-74 was flaky and the phosphating treatment provided favourable conditions for $BiVO_4$ growth. Fig. 2(b) shows the morphology change after phosphating NiMOF-74. Apart from developing a roughened surface, the phosphated product Ni-MOF/P preserved the basic morphology of Ni-MOF-74. Meanwhile, tiny nanoparticles formed on the surface of the rhombic structure, proving the XRD observation of Ni_2P. In addition, bare $BiVO_4$ presented a peanut-like morphology (Fig. 2(c)) with an average size of approximately 1.5 μm (Fig. 2(c), inset). The sizes of $BiVO_4$ and Ni_2P conform to the assumed of Ni-MOF-74 is the growth substrate. The morphology of 20-NBP was shown in Fig. 2(d). The material maintained the rhombic structure of Ni-MOF-74 but its lamellar structure was looser, facilitating the adhesion of Ni_2P nanoparticles and $BiVO_4$. In addition, the peanut-like $BiVO_4$ closely contacted with Ni-MOF-74 and Ni_2P to form an interface. These results further illustrate that the metal-organic framework provides a support substrate for the growth and close contact of Ni_2P and $BiVO_4$, which is beneficial to the separation and transport of the carriers.

The morphology of Ni-MOF-74, $BiVO_4$ and 20-NBP were deeply explored through transmission electron microscopy (TEM). As shown in Fig. 3(a,b), the morphologies of Ni-MOF-74 and $BiVO_4$ were consistent in the SEM images. After magnifying the TEM image of 20-NBP, the morphological characteristics of Ni-MOF-74, $BiVO_4$ and Ni_2P became

apparent (Fig. 3(c,d)). The loose pore structure of Ni-MOF-74 in the TEM image confirms that Ni-MOF-74 can be used as growth substrate for $BiVO_4$ and Ni_2P. In addition, the high-resolution TEM image shows that the material has clear lattice fringes. In Fig. 3(e), the lattice spacing value of $BiVO_4$ was detected to be 0.46 nm, which belongs to its (101) crystal plane. The spacing of 0.19 nm, 0.31 nm and 0.22 nm corresponded to the (204), (112) and (211) crystal planes of $BiVO_4$, respectively whereas those at 0.20 nm, corresponded to the (021) crystal planes of Ni_2P, respectively (Fig. 3 (f)). The lattice spacing corresponding to Ni-MOF-74 were absent because it was destroyed by the electron beam during the test. To further prove the successful preparation of the photocatalyst, the element distributions in 20-NBP were analysed by elemental mapping (Fig. 3(g)). The distributions of Ni, Bi, V, O and P elements were consistent with the EDX results. Fig. 3(h) shows the SEM image of 20-NBP after continuous hydrogen evolution for 5 h. Obviously, its morphology did not change much before and after the hydrogen evolution experiment.

3.3. X-ray photoelectron spectroscopy

The surface chemical valences and elemental compositions of Ni-MOF-74, Ni-MOF/P, $BiVO_4$ and Ni-MOF-74/$BiVO_4$ were analysed by XPS. Fig. 4(a) shows the full-spectrum XPS information of the samples. The presence of Ni, Bi, V, O, and C elements affirmed the successful combination of rhombic structure Ni-MOF-74 with peanut-like $BiVO_4$. Fig. 4(b) shows the fine spectra of the Ni elements in Ni-MOF-74 and Ni-MOF-74/$BiVO_4$. The binding energies at 856.39 eV and 874.08 eV in the spectrum of pure Ni-MOF-74 were contributed by Ni $2p_{3/2}$ and Ni $2p_{1/2}$,
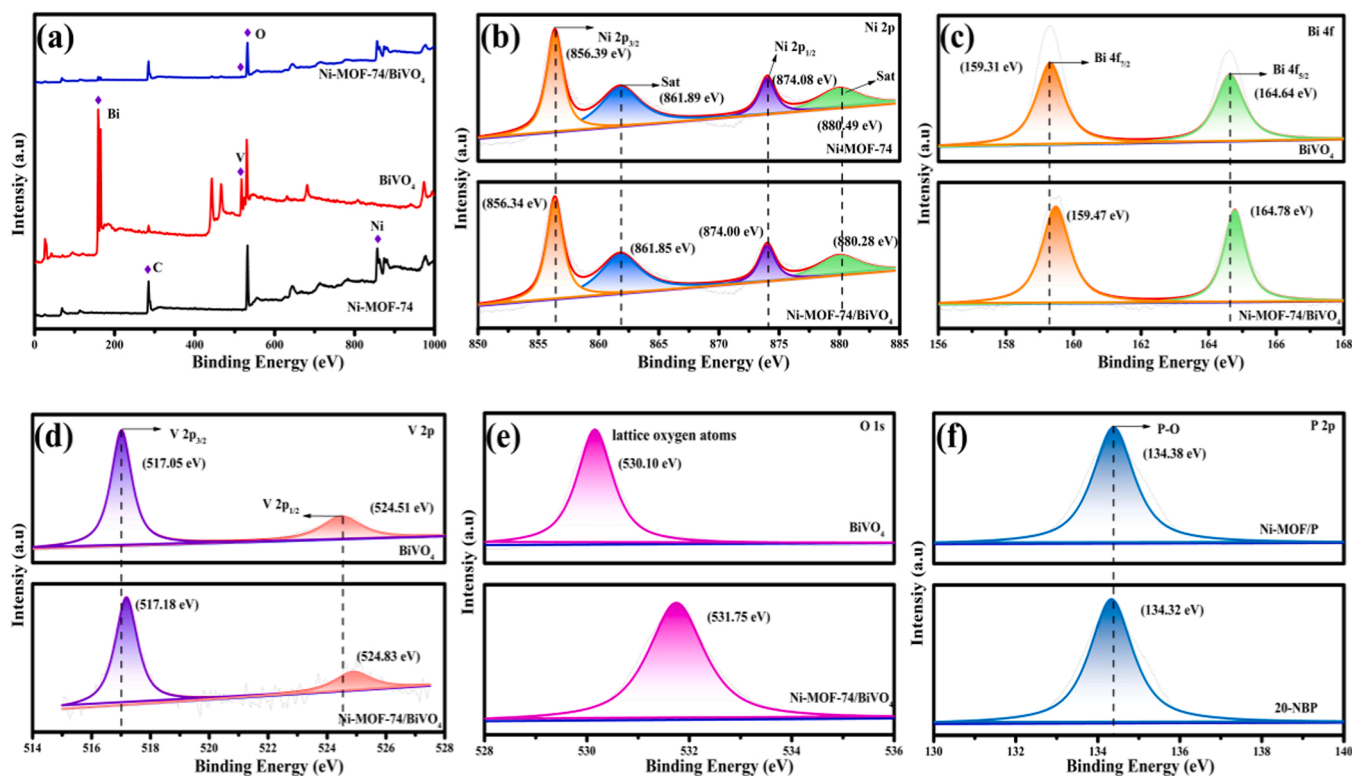
Fig. 4. XPS results (a) survey spectra and (b) Ni 2p; (c) Bi 4f; (d) V 2p; (e) O 1s and (f) P 2p spectra of the prepared samples.

respectively [41,42]. The two satellite peaks at 861.89 eV and 880.49 eV were attributed to surface oxidation of Ni^{2+} [43]. The slight change of the Ni binding energy in Ni-MOF-74/BiVO$_4$ from that of Ni-MOF-74 indicates a strong interaction between the materials. In the high-resolution XPS spectrum of Bi element in pure BiVO$_4$, the peak binding energies at 159.31 eV and 164.64 eV could be assigned to Bi $4f_{7/2}$ and Bi $4f_{5/2}$, respectively (Fig. 4(c)) [44]. The fine spectrum of V (Fig. 4(d)) also showed two peaks, but with binding energies of 517.05 eV and 524.51 eV attributable to V $2p_{3/2}$ and V $2p_{1/2}$, respectively. This result confirms the presence of V^{5+} ions in BiVO$_4$ [45]. Fig. 4 (e) shows the fine spectra of O elements in BiVO$_4$ and Ni-MOF–74/BiVO$_4$. A lattice oxygen peak with a binding energy of 530.10 eV was detected in pure BiVO$_4$ [46]. In contrast, the O 1s spectrum of Ni-MOF–74/BiVO$_4$ has a lattice oxygen (O^{2-}) peak with a binding energy of 531.75eV [47]. Finally, the fine spectrum of the P element (Fig. 4(f)) presented a binding energy peak at 134.38 eV, indicating that phosphate was oxidised when Ni-MOF/P was exposed to air [48]. The binding energy of the P element decreased slightly in 20-NBP, again reflecting strong interaction between the materials in the composite.

3.4. Brunauer–Emmett–Teller (BET) analysis

Fig. 5 shows the nitrogen adsorption-desorption curves of Ni-MOF-74, Ni-MOF/P, BiVO$_4$ and 20-NBP. In the International Union of Pure and Applied Chemistry (IUPAC) classification, the isotherm of the sample was a typical IV curve and an obvious H3 hysteresis loop appeared at relative pressures (P/P$_0$) of 0.8–1.0 [49]. In Table 2, the specific surface area, pore volume and average pore size distribution data of the materials are included. The pore size distribution of the sample ranges from 2 nm to 50 nm, which is a typical mesoporous material [50]. After phosphating treatment of Ni-MOF-74 (9 m^2 g^{-1}) under high temperature calcination conditions, the specific surface area of Ni-MOF-74/P increased by a small extent (15 m^2 g^{-1}), possibly because the surface flaky structure was deformed by the

high-temperature calcination, and the structure of the metal-organic framework become fluffy. The increased specific surface area exposed more active sites that participated in the water splitting reaction, consistent with the higher hydrogen production activity of Ni-MOF/P than of Ni-MOF-74. Although the surface area of 20-NBP (5 m^2 g^{-1}) was reduced as BiVO$_4$ accumulated growth on the Ni-MOF-74 surface, the role of Ni-MOF-74 as the base material was maintained. The above results indicate that the pore structure and specific surface area are important determiners of photocatalytic activity, but are not the main factors.

3.5. Hydrogen evolution of the photocatalyst

The performances of the photocatalysts were determined in a hydrogen production kinetic test [51]. Fig. 6(a) displays the hydrogen production performance of Ni-MOF-74, Ni-MOF/P, BiVO$_4$ and 20-NBP. The hydrogen-production performance of Ni-MOF-74 alone was infeasible for practical applications, while the efficiency of BiVO$_4$ was limited by the poor internal charge transfer characteristics, and the hydrogen production activity was almost weak. Conversely, the hydrogen generation ability of Ni-MOF/P was boosted by the large number of negative charges, which attracted electrons for the reduction reaction. Therefore, Ni-MOF/P showed better hydrogen production activity than pure Ni-MOF-74. The composite photocatalyst exhibited the highest hydrogen-production activity because construction of the S-scheme heterojunction between Ni-MOF-74 and BiVO$_4$ directed the carrier transport. Fig. 6(b) shows the hydrogen evolution kinetic results of Ni-MOF-74/BiVO$_4$ and x-NBP obtained over five hours. 20-NBP achieved the highest hydrogen production activity, reaching 245.4 μmol in five hours (23 times that of pure Ni-MOF-74). Increasing the BiVO$_4$ content gradually increased the hydrogen production activity of the composite photocatalyst until the BiVO$_4$ content is higher than 20%. It was surmised that when excessive BiVO$_4$ accumulated on the surface of Ni-MOF-74, the pores of the framework were blocked the contact with water molecules was reduced. The hydrogen production kinetics were
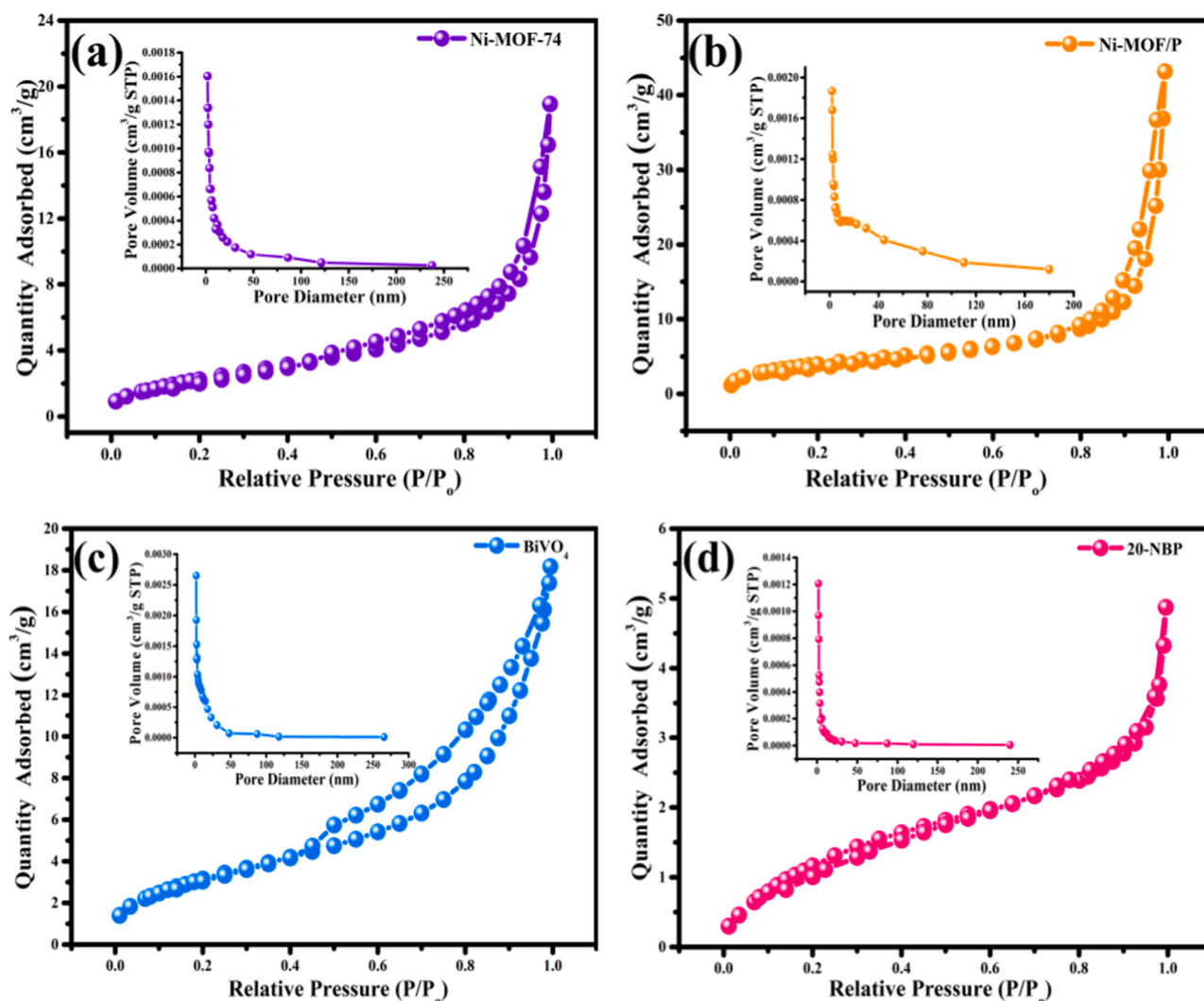
Fig. 5. N_2 adsorption–desorption isotherms and pore diameter distribution curves of (a) Ni-MOF-74; (b) Ni-MOF/P; (c) $BiVO_4$ and (d) 20-NBP.

Table 2
S_{BET}, pore volumes and average pore diameter distributions of the samples.

Samples	S_{BET} ($m^2\,g^{-1}$)[a]	Pore volume ($cm^3\,g^{-1}$)[b]	Average pore size (nm)[b]
Ni-MOF-74	9	0.03	13.55
Ni-MOF/P	15	0.06	21.14
$BiVO_4$	12	0.03	9.53
20-NBP	5	0.01	7.43

[a] Obtained by the BET method.
[b] Relative pressure (P/P_0) = 0.99.

also greatly affected by the amount of dye sensitiser in the reaction. To investigate this effect the EY in the photocatalytic water splitting reaction was varied without changing the amounts of catalyst and sacrificial reagent. In the reaction with an EY dosage of 15 mg, the hydrogen production reached 163.17 μmol in five hours (Fig. 6(c)). However, when the amount of EY reaches 25 mg, the hydrogen evolution performance decreases, indicating that too much EY content is not conducive to the progress of photocatalytic activity. To further refine the experimental conditions, the phosphating degree ($NaH_2PO_2 \cdot H_2O$ amount) of 20-NBP was changed and the results are plotted in Fig. 6(d). The hydrogen evolution activity of 20-NBP was maximised when the $NaH_2PO_2 \cdot H_2O$ amount was five times that of Ni-MOF-74.

In addition, excessive accumulation of EY in the entire system will mask the active sites of the samples and greatly affect the stability of the photocatalyst. As shown in Fig. 7(a), 20-NBP can maintain good hydrogen evolution performance in two cycles after adding fresh EY (20 mg). However, the activity of the material in the third cycle decreased significantly under the same conditions of adding fresh EY. This phenomenon can be attributed to the degradation of EY and the consumption of sacrificial reagents in a long-term light environment [52]. Therefore, the catalyst after the third cycle was washed with deionized water and dried to obtain powder. The same operation procedure as the hydrogen evolution experiment was carried out, and fresh sacrificial reagents and sensitizers were added to find that its activity was significantly increased. Comparing the X-ray diffraction spectra of 20-NBP after zero and five hours of hydrogen production the basic crystal phase structure was preserved after hydrogen production even though the peaks of the individual diffraction peaks were weakened (see Fig. 7(b)). In addition, the illustration shows that the hydrogen evolution activity of the material after drying has decreased, but it is not serious. In order to further confirm the stability of 20-NBP, the XPS spectra of before and after the hydrogen evolution experiment were compared (in Fig. 7(c–f)). Among them, the peaks in the full spectrum and fine spectrum of the elements did not change significantly, showing the good stability of 20-NBP. To further demonstrate the improved hydrogen production performance of the proposed composite material, our hydrogen-production rates are compared with those of previously reported data in Table 3.
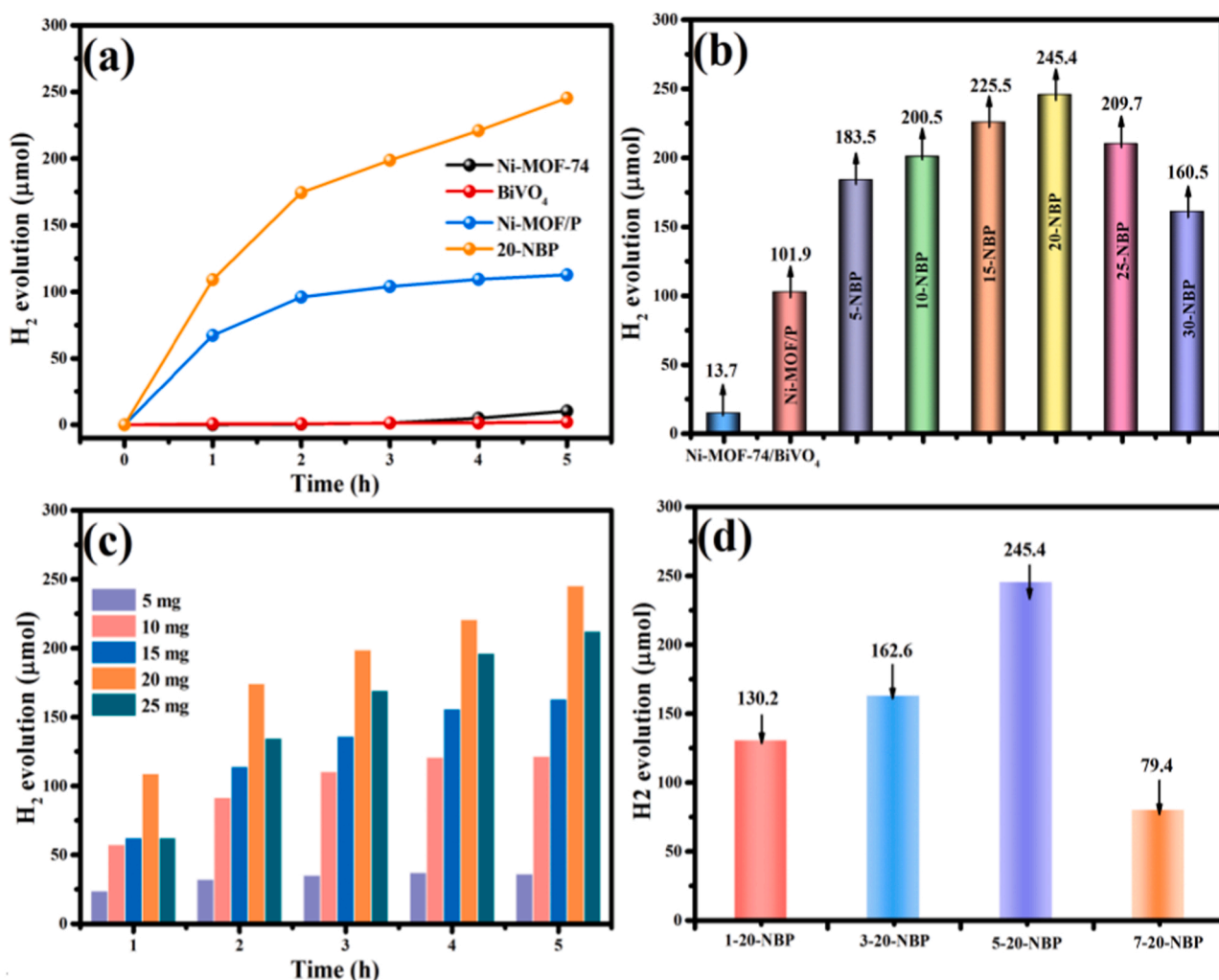
Fig. 6. (a) Photocatalytic H_2 evolution performances of Ni-MOF-74, Ni-MOF/P, BiVO$_4$ and 20-NBP; (b) H_2 evolution rates of x-NBP under visible light irradiation; effects of (c) EY and (d) NaH$_2$PO$_2$·H$_2$O amount on hydrogen production activity of 20-NBP.

3.6. UV–vis diffuse reflectance absorption analysis (DRS)

The light absorption properties of Ni-MOF-74, Ni-MOF/P, BiVO$_4$ and 20-NBP were obtained from UV–vis diffuse reflectance. As shown in Fig. 8(a), the absorption capacity of rhombic structure Ni-MOF-74 was non-ideal [53]. Different from other semiconductor materials, Ni-MOF-74 has two absorption edges: an intrinsic absorption band edge at 400–500 nm and an absorption band at 600–700 nm in the boundary region due to charge transfer from the 2p orbitals of oxygen to the 3d orbitals of Ni^{2+} ions [54]. Peanut-like BiVO$_4$ presented a similar absorption band edge at 530 nm and a higher visible-light absorption capacity than Ni-MOF-74. Phosphated Ni-MOF-74 exhibited the unique light absorption properties of black material, with a linear presentation of the absorption spectrum. The absorption performance of 20-NBP is higher than that of Ni-MOF-74 and BiVO$_4$ due to the similar black material properties of Ni-MOF/P. Therefore, the phosphating treatment strategy and the EY sensitization system can effectively improve the utilisation efficiency of the catalyst for visible light.

The bandgap energy of Ni-MOF-74 and BiVO$_4$ were calculated by Eq. (1):

$$ah\nu = A\left(h\nu - E_g\right)^{\frac{n}{2}}\tag{1}$$

Where a, $h\nu$, E_g and A denote the absorption coefficient, photon energy, bandgap energy and a constant, respectively.

The bandgap values of Ni-MOF-74 and BiVO$_4$ were 2.4 eV and 2.3 eV, respectively (Fig. 8(b)) [54]. From the above discussion, it was concluded that the band gap values of both semiconductor materials could be excited by light to generate carriers.

3.7. Photoluminescence analysis

The separation and transfer of electrons determine the photocatalyst performance of the photocatalyst. Therefore, the electron separation was studied by PL spectroscopy. The samples exhibited a similar fluorescence emission peak at 530 nm (Fig. 9(a)). As is well-known, the intensity of the emission peak represents the recombination degree of electron-hole pairs. The rebound quenching of excited state electrons in the EY solution manifested as strong fluorescence emission. The intensities of the diffraction peaks of Ni-MOF-74, Ni-MOF/P, BiVO$_4$ and 20-NBP were significantly lower than those of pure EY solution. The fluorescence peaks of 20-NBP showed the lowest intensity, indicating suppression of the internal electron-hole recombinations. The second-lowest intensity was shown by Ni-MOF/P, demonstrating that the good metal-like properties of Ni$_2$P accelerated the efficient transfer of excited state electrons and promoted their participation in the photocatalytic water splitting reaction.

Next, the carrier lifetimes of the samples were analysed using the data shown in Table 4. Based on double exponential decay kinetics fitting formula, the decay curves and lifetimes of the samples were
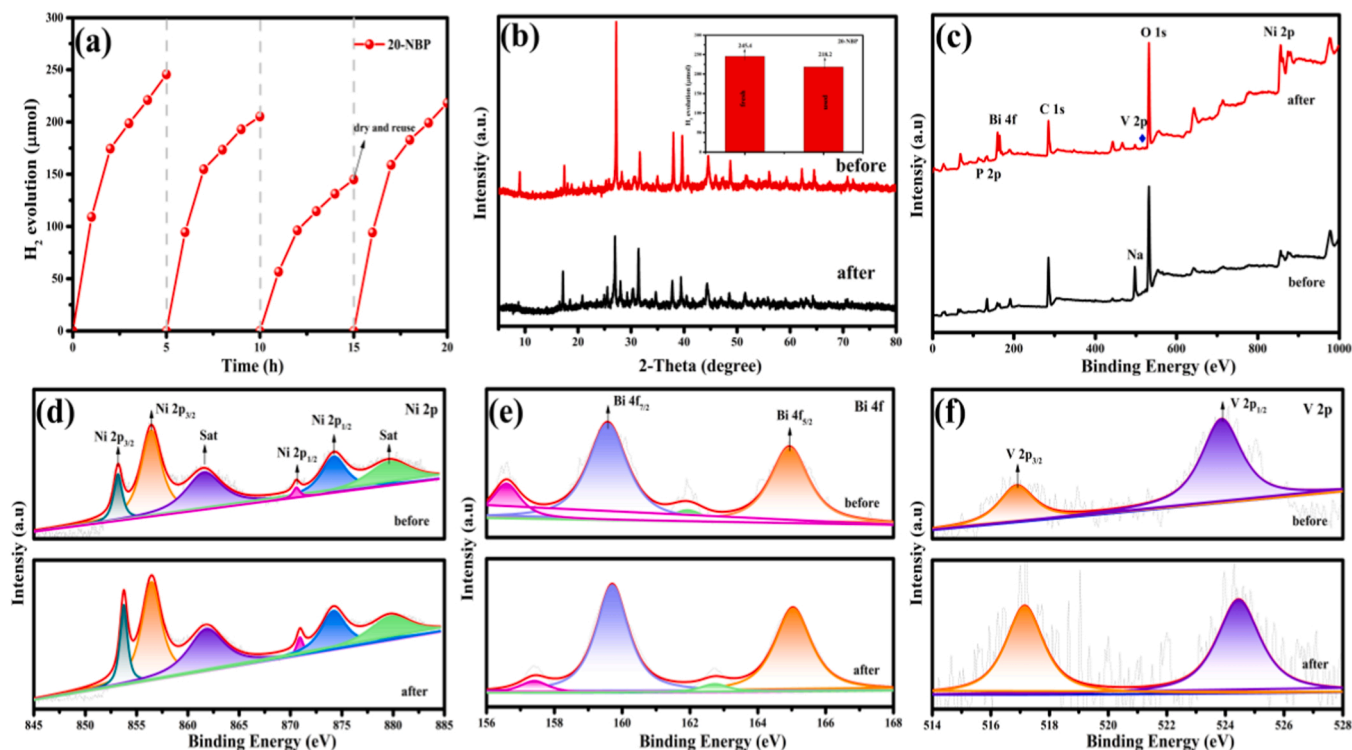
Fig. 7. (a) cyclic stability experiments of 20-NBP; (b) X-ray diffraction patterns and XPS results (c) survey spectra and (d) Ni 2p; (e) Bi 4f; (f) V 2p of 20-NBP before and after the hydrogen evolution reaction.

Table 3
Hydrogen production rates of Ni-MOF-74/BiVO$_4$/P and Ni$_2$P photocatalysts reported in the literature.

Photocatalyst	Light Source	Sacrificial agents	Production rate	Refs
Ni-MOF-74/ BiVO$_4$/P	5 W LED ($\lambda \geq$ 420 nm)	Trolamine	4908 µmol h^{-1} g^{-1}	Here
g-C3N$_4$/Ni$_2$P	300 W Xenon lamp ($\lambda >$ 420 nm)	Trolamine	270 µmol h^{-1} g^{-1}	[19]
Ni$_2$P/g-C$_3$N$_4$	300 W Xe lamp ($\lambda \geq$ 420 nm)	Trolamine	362.4 µmol h^{-1} g^{-1}	[5]
Ni$_2$P/red P	300 W Xe lamp ($\lambda \geq$ 420 nm)	Methanol (10 vol%)	265.4 µmol h^{-1} g^{-1}	[22]
g-C3N$_4$/Ni$_2$P	300 W Xe lamp ($\lambda \geq$ 420 nm)	Trolamine	567 µmol h^{-1} g^{-1}	[20]

obtained to the following formulate (Eqs. (2) and (3)) [55].

$$I(t) = \sum_{i=1,2} A_i e^{-t/\tau_i} \tag{2}$$

$$<\tau_{ave}> = \frac{\sum_{i=1,2} A_i \tau_i^2}{\sum_{i=1,2} A_i \tau_i} \tag{3}$$

where τ_1 and τ_2 are the emission lifetimes and A is the corresponding amplitude.

In general, a change in the carrier lifetime indicates a modification of the electron transport or electron band (Fig. 9(b)). The carrier lifetime is composed of a non-radiative process (τ_1) and a radiation process (τ_2). The radiation process (τ_2) is strongly related to recombination of the photo-generated electron-hole pairs [56]. The short life of 20-NBP is 0.34 ns compared to the EY solution, although its percentage has only increased from 92.67% to 95.82%. From the double exponential fitting, the average lifetime of EY was determined as 0.26 ns. The average lifetime is considered to roughly estimate the efficiency of light-generated charge separation [57]. The longer the average life of

the catalyst, the slower is the photo-induced carrier recombination. In the data analysis, 20-NBP exhibited the longest average life (0.33 ns), indicating that the S-scheme heterojunction and the Ni$_2$P electron capture centers between the semiconductors greatly extended the life of the carriers, enabling their maximal participation in the photocatalytic cracking water reaction. The structure also enforces directional control of the carrier transmission path. The significantly extended average carrier lifetime indicates that the single excited-state lifetime of EY[1*] was also extended, thus promoting the production of stable EY[3*]. Under the action of TEOA, EY[3*] was converted into EY$^{..}$ and injected into the catalyst for the photocatalytic reaction.

3.8. Electrochemical characterization

The electrochemical performances of Ni-MOF-74, BiVO$_4$, Ni-MOF/P and 20-NBP are shown in Fig. 10. The photocurrent responses revealed the charge separation and transfer processes of the samples in detail. As shown in Fig. 10(a), 20-NBP showed a better photocurrent response, confirming that the separation and migration of internal carriers in this photocatalyst has been improved. Among the samples, 20-NBP presented the smallest interface resistance (Fig. 10(b)), indicating the lowest resistance to electron transport. In general, a low resistance at the interface facilitates the separation and transfer of charge [58]. The improved conductivity of the composite material was attributed to the metal-like properties of Ni$_2$P. Therefore, the improvement of internal electron transport in 20-NBP has been confirmed in electrochemical tests and fluorescence spectroscopy.

The hydrogen evolution overpotentials and current densities of the materials were tested using linear sweep voltammetry in Fig. 10(c). The hydrogen evolution overpotential of the photocatalyst strongly affected the hydrogen evolution performance of the material. The lower overpotential of 20-NBP than of the other materials, corresponded to the strongest photocatalytic activity of 20-NBP. The reduction of the overpotential of the composite catalyst is due to the contact interface and heterojunction between the materials, which facilitate the rapid transfer
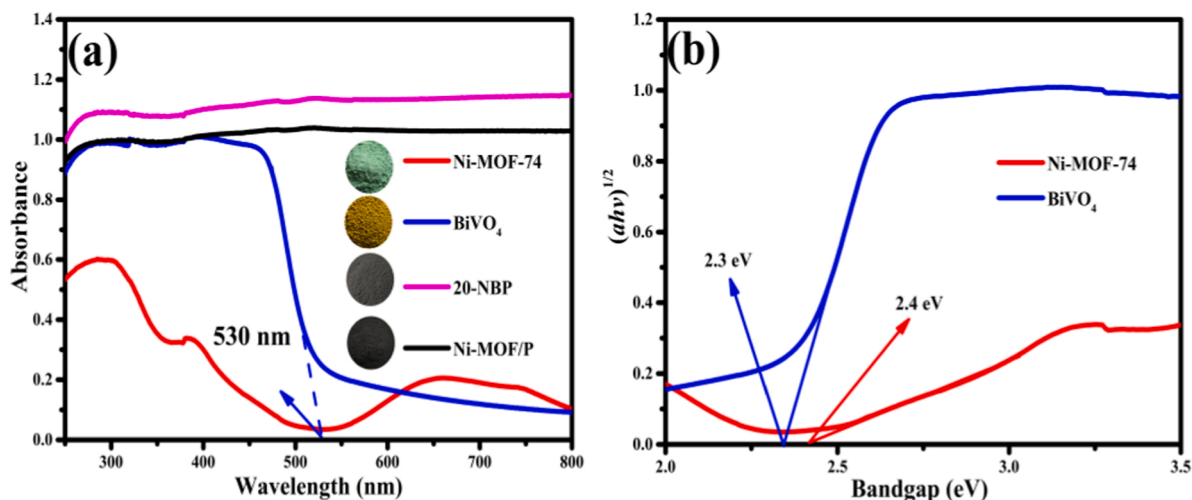
Fig. 8. (a) UV–vis DRS spectra of Ni-MOF-74, BiVO$_4$, Ni-MOF/P and 20-NBP; (b) Forbidden band widths of Ni-MOF-74 and BiVO$_4$.
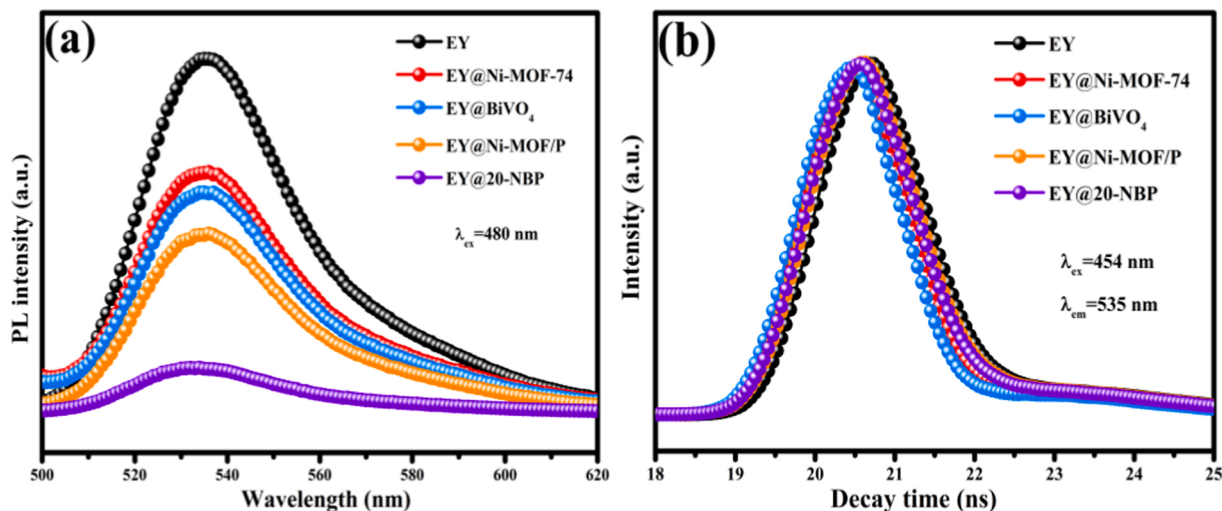

Fig. 9. (a) PL spectra and (b) time-resolved fluorescence spectra of EY, EY@Ni-MOF-74, EY@BiVO$_4$, EY@Ni-MOF/P and EY@20-NBP.

Table 4
Kinetic analysis of emission decays of EY, EY@Ni-MOF-74, EY@BiVO$_4$, EY@Ni-MOF/P and EY@20-NBP.

Samples	Lifetime $<\tau>$(ns)	Pre-exponential Factors A%	Average lifetime $<\tau_{av}>$(ns)[b]	X^2
EY	$\tau_1 = 0.24$	92.67%	0.26	1.25
	$\tau_2 = 4.53$	7.33%		
Ni-MOF-74	$\tau_1 = 0.11$	98.30%	0.11	1.49
	$\tau_2 = 5.56$	1.70%		
BiVO$_4$	$\tau_1 = 0.23$	92.83%	0.25	1.22
	$\tau_2 = 4.43$	7.17%		
Ni-MOF-74/P	$\tau_1 = 0.18$	97.35%	0.19	1.32
	$\tau_2 = 3.84$	2.65%		
20-NBP	$\tau_1 = 0.34$	95.82%	0.33	1.23
	$\tau_2 = 4.07$	4.18%		

of electrons. Consequently, the overpotential of 20-NBP is also one of the factors that increase the hydrogen production activity.

In Fig. 10(d–f), the Mott-Schottky curves of Ni-MOF-74, BiVO$_4$ and Ni-MOF/P were tested under 500 Hz, 800 Hz and 1000 Hz. The flat band potentials of Ni-MOF-74, BiVO$_4$ and Ni-MOF/P were − 0.87 eV, − 0.54 eV and − 0.52 eV, respectively (Eq. (4)).

$$\frac{1}{C^2} = 2(N_D e \varepsilon \varepsilon_0)^{-1} \bullet \left(\text{E} - E_{fb} - \frac{kT}{e} \right) \tag{4}$$

where C is the capacitance of the space charge region; N_D is the charge carrier concentration; e is the electron charge; ε is dielectric constant; ε_0 is the vacuum permittivity; E is the electrode applied potential; E_{fb} is the flat band potentials; K is the Boltzmann constant and T is the absolute temperature.

The Mott-Schottky curves can also be used to determine the types of semiconductors. When the slope of the curve is positive, the material is an n-type semiconductor [59]. Moreover, the conduction band (CB) positions of Ni-MOF-74, BiVO$_4$ and Ni-MOF/P can be roughly obtained based on the flat-band potentials of the materials. In previous reports of n-type semiconductors, the CB potential was 0.1–0.2 eV more negative than the flat band potential [60]. The CB values of Ni-MOF-74, BiVO$_4$ and Ni-MOF/P were − 0.83 eV, − 0.50 eV and − 0.48 eV, respectively (Eq. (5)). The valence bands (VB) of the Ni-MOF-74 and BiVO$_4$ semiconductor, from which the possible mechanism of composite materials can be deduced, were determined from the corresponding band gaps and Eq. (6). The data were shown in Table 5.

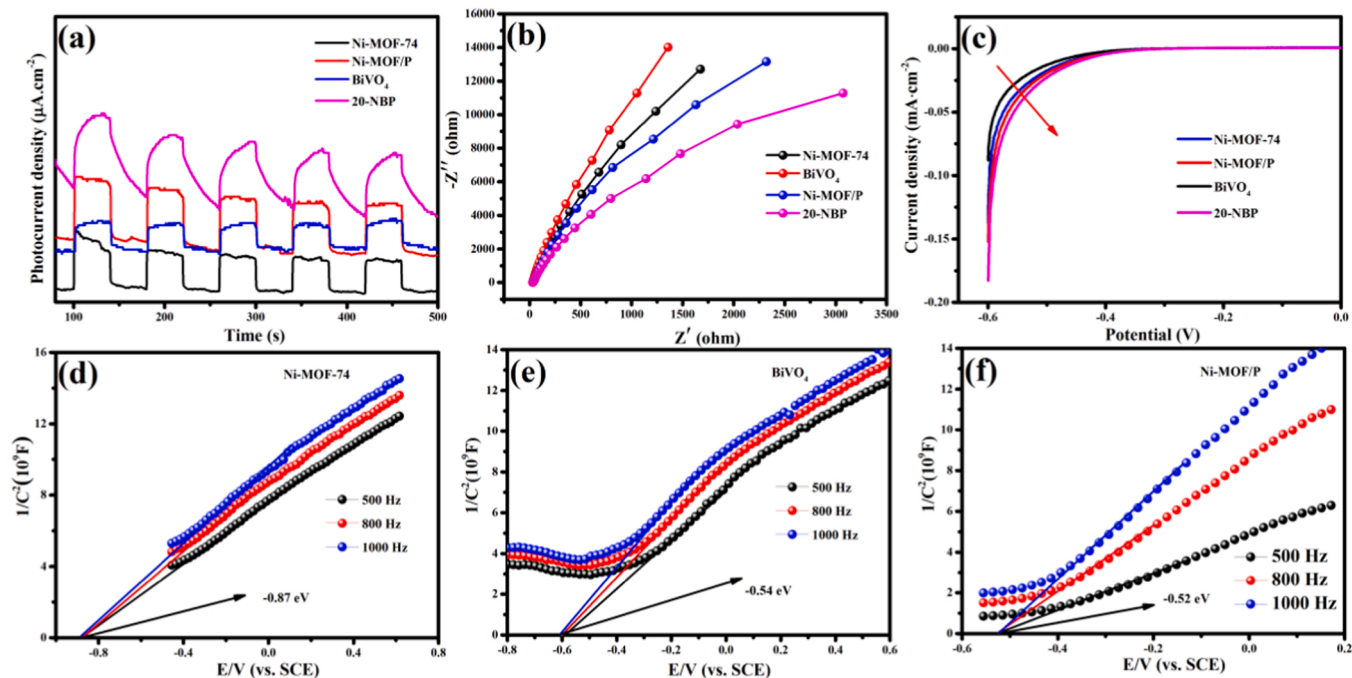$$E_{NHE} = E_{SCE} + 0.24 \quad eV \tag{5}$$

Fig. 10. (a) Transient photocurrent responses; (b) Nyquist plots and (c) LSV curves of Ni-MOF-74, BiVO$_4$, Ni-MOF/P and 20-NBP; (d–f) Mott-Schottky plots of Ni-MOF-74, BiVO$_4$ and Ni-MOF/P.

Table 5
Calculated CB and VB positions of Ni-MOF-74 and BiVO$_4$.

Samples	Band energy E$_g$ (eV)	Valence band E$_{VB}$ (eV)	Conduction band E$_{CB}$ (eV)
Ni-MOF-74	2.4	1.57	-0.83
BiVO$_4$	2.3	1.80	-0.50

$$E_{CB} = E_{VB} - E_g \tag{6}$$

Fig. 11(a, b) shows the optimized structure models of Ni$_2$P and BiVO$_4$, respectively. In order to ensure a reasonable distribution of the material band gap, the U values of Ni and V were set to 3.8 eV and 2.7 eV, respectively [61,62]. Fig. 11(c, d) shows the band structure of Ni$_2$P and BiVO$_4$ obtained by density functional calculation. Ni$_2$P was identified as a metal-like material with excellent electrical conductivity and no direct band gap, further proving that the excellent conductivity
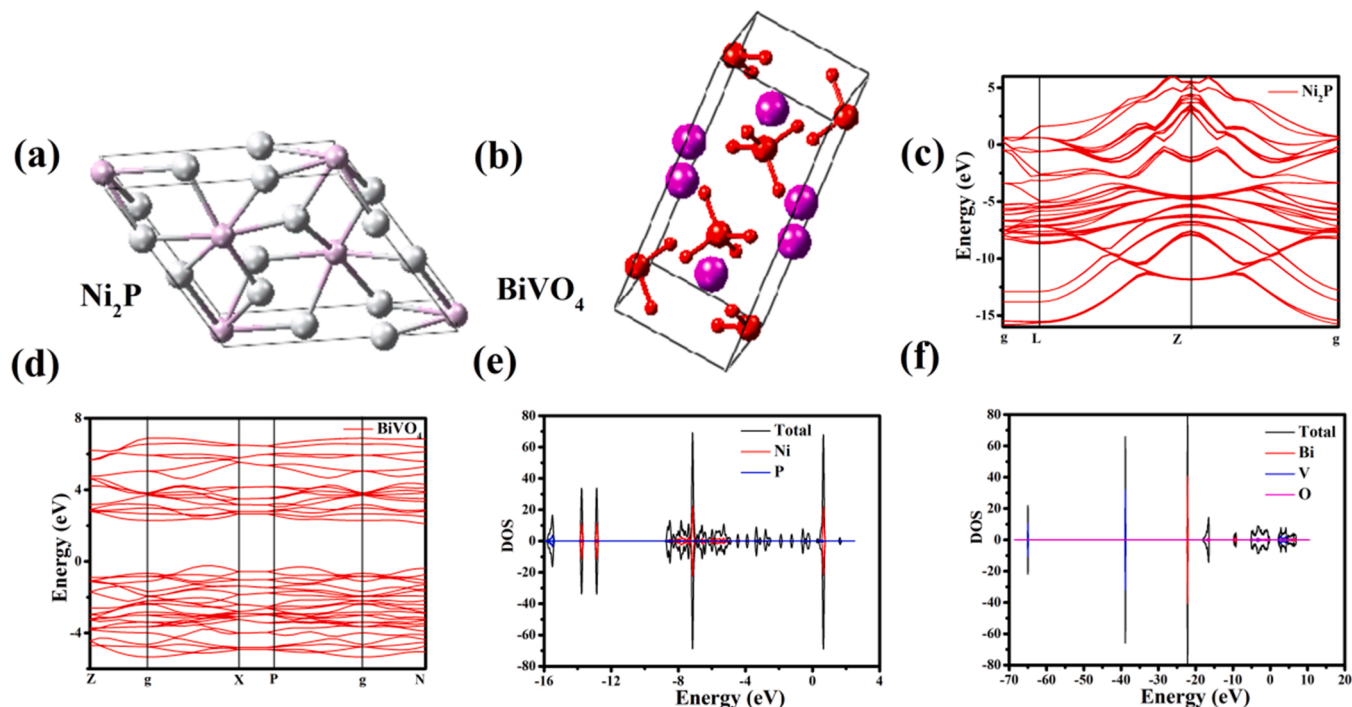

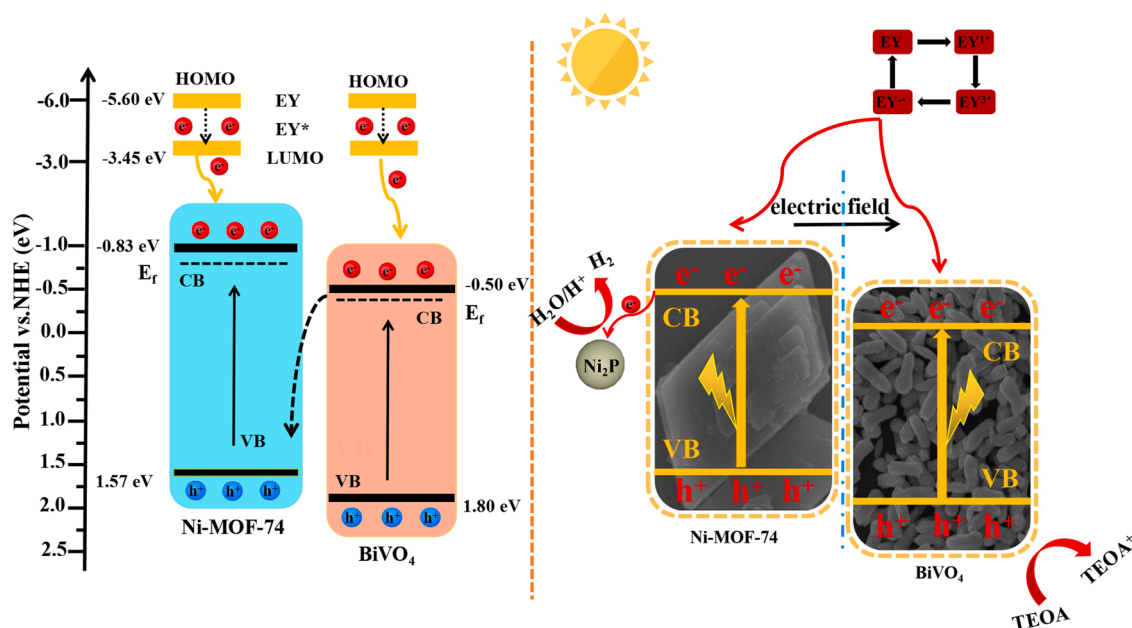**Fig. 11.** (a,b) Model structures; (c,d) band structures and; (e,f) density of states of Ni$_2$P and BiVO$_4$.

Fig. 12. Mechanism of Ni-MOF-74/BiVO$_4$/P.

of Ni$_2$P can strongly support for the improvement of the conductivity of the whole system. The calculated indirect band gap of BiVO$_4$ was 2.304 eV, which is similiar to the band gap obtained from the ultraviolet diffuse reflection test and the values reported in the literature [63]. Fig. 11(e, f) shows the calculated density of states diagrams of Ni$_2$P and BiVO$_4$. The high density of electronic states near the Fermi level in Ni$_2$P was consistent with the metal-like properties and good conductivity of Ni$_2$P [64]. Analyzing the density of states map of BiVO$_4$, VB was mainly composed of the O 2p state, whereas the CB was mainly composed of the V 3d, O 2p and Bi 6p states [65].

3.9. Possible photocatalytic mechanism over Ni-MOF-74/BiVO$_4$/P

Fig. 12 shows the possible reaction mechanism of Ni-MOF-74/BiVO$_4$/P. The photocatalyst enlarges the spectral response region of the wide bandgap semiconductor in the dye-sensitive system. The EY molecules in the bound state are adsorbed on the catalyst surface and form a single excited state EY^{1*} after absorbing energy from the simulated light. The excited EY^{1*} is unstable and transforms into EY^{3*}, which is reductively quenched and transformed into a more reductive EY$^{-\bullet}$ state with TEOA as the electron donor [66]. The strong interaction between the EY molecule and the material can promote the reaction. Under visible-light excitation, the electrons in the VBs of Ni-MOF-74 and BiVO$_4$ are excited and transferred to the CBs, thereby separating the electrons and holes. Unlike the situation in previous heterojunction structures, the potential energy difference drives the recombination of the useless electrons in the CB of BiVO$_4$ with the holes in the VB of Ni-MOF-74. Meanwhile, the electrons in the CB of Ni-MOF-74 are retained to participate in the reaction [29]. In conclusion, the formation conditions of the S-scheme heterojunction are satisfied and the recombination of electron-hole pairs is effectively suppressed [67]. In addition, the CB position is lower in the Ni$_2$P nanoparticles than in Ni-MOF-74 and electrons can be retrieved for the redox reaction. The holes remaining in the BiVO$_4$ can be consumed by TEOA to form TEOA$^+$.

4. Conclusion

In summary, the Ni-MOF-74/BiVO$_4$/P with excellent performance can be obtained by high temperature calcination method. The metal-organic framework of Ni-MOF-74 provided the support material for

Ni$_2$P and BiVO$_4$. The porous structure improves the electron transfer path, and the and derivative Ni$_2$P particles act as electron capture centres to enhance the attraction of electrons. The excellent performance of 20-NBP was reflected in the hydrogen production activity, which reached 245.4 μmol. In addition, the heterojunction and metal-like Ni$_2$P effectively transferred the charge carriers and avoided their recombination with holes. Through the ultraviolet diffuse reflectance test, fluorescence spectroscopy and electrochemistry, it is confirmed that the composite material has an enhanced ability to absorb visible light and the transfer of electrons is effectively regulated. This work provides new ideas for constructing heterojunctions with metal organic framework supports for the directional control of carrier transfer.

CRediT authorship contribution statement

Zhiliang Jin: designed the experiments, contributed reagents/materials and analysis tools. **Hongying Li:** designed the experiments, wrote the paper. **Haiming Gong:** assisted in the partial testing of the experiment.

Declaration of Competing Interest

The authors declare that they have no known competing financial interests or personal relationships that could have appeared to influence the work reported in this paper.

Acknowledgements

Author contributions

Hongying Li designed the experiments, Zhiliang Jin contributed reagents/materials and analysis tools; Haiming Gong assisted in the partial testing of the experiment; Hongying Li wrote the paper.

References

[1] J. Chen, J. Yi, W. Zhu, W. Zhang, T. An, Oxygen isotope tracing study to directly reveal the role of O_2 and H_2O in the photocatalytic oxidation mechanism of gaseous monoaromatics, Environ. Sci. Technol. 55 (2021) 16617–16626.

[2] Y. Li, R. He, P. Han, B. Hou, S. Peng, C. Ouyang, A new concept: volume photocatalysis for efficient H_2 generation-Using low polymeric carbon nitride as an example, Appl. Catal. B–Environ. 279 (2020), 119379.

[3] M. Zhang, Q. Hu, K. Ma, Y. Ding, C. Li, Pyroelectric effect in CdS nanorods decorated with a molecular Co–catalyst for hydrogen evolution, Nano Energy 73 (2020), 104810.

[4] X. Jiang, H. Gong, Q. Liu, M. Song, C. Huang, In situ construction of NiSe/ $Mn_{0.5}Cd_{0.5}S$ composites for enhanced photocatalytic hydrogen production under visible light, Appl. Catal. B–Environ. 268 (2020), 118439.

[5] W. Wang, T. An, G. Li, D. Xia, H. Zhao, J. Yu, P. Wong, Earth-abundant $Ni_2P/$ g–C_3N_4 lamellar nanohydrids for enhanced photocatalytic hydrogen evolution and bacterial inactivation under visible light irradiation, Appl. Catal. B-Environ. 217 (2017) 570–580.

[6] J. Lin, P. Li, H. Xu, Y. Kim, Z. Jing, D. Zheng, Controlled synthesis of mesoporous single–crystalline TiO_2 nanoparticles for efficient photocatalytic H_2 evolution, J. Hazard. Mater. 391 (2020), 122530.

[7] Z. Jiang, Q. Chen, Q. Zheng, R. Shen, P. Zhang, X. Li, Constructing 1D/2D schottky-based heterojunctions between $Mn_{0.2}Cd_{0.8}S$ nanorods and Ti_3C_2 nanosheets for boosted photocatalytic H_2 evolution, Acta Phys. Chim. Sin. 37 (2021), 2010059.

[8] N. Tang, Y. Li, F. Chen, Z. Han, In situ fabrication of a direct Z-scheme photocatalyst by immobilizing CdS quantum dots in the channels of graphene-hybridized and supported mesoporous titanium nanocrystals for high photocatalytic performance under visible light, RSC Adv. 8 (2018) 42233–42245.

[9] R. He, R. Chen, J. Luo, S. Zhang, D. Xu, Fabrication of graphene quantum dots modified BiOI/PAN flexible fiber with enhanced photocatalytic activity, Acta Phys. Chim. Sin. 37 (2021), 2011022.

[10] X. Ding, H. Liu, J. Chen, M. Wen, G. Li, T. An, H. Zhao, In situ growth of well-aligned Ni-MOF nanosheets on nickel foam for enhanced photocatalytic degradation of typical volatile organic compounds, Nanoscale 12 (2020) 9462–9470.

[11] S. Dang, Q. Zhu, Q. Xu, Nanomaterials derived from metal–organic frameworks, Nat. Rev. Mater. 3 (2017) 1–14.

[12] A. Mahmood, W. Guo, H. Tabassum, R. Zou, Metal–organic framework-based nanomaterials for electrocatalysis, Adv. Energy Mater. 6 (2016), 1600423.

[13] X. He, M. Wu, Z. Ao, B. Lai, Y. Zhou, T. An, S. Wang, Metal–organic frameworks derived C/TiO_2 for visible light photocatalysis: simple synthesis and contribution of carbon species, J. Hazard. Mater. 403 (2021), 124048.

[14] Y. Tang, M. Gao, C. Liu, S. Li, H. Jiang, Y. Lan, M. Han, S. Yu, Porous molybdenum–based hybrid catalysts for highly efficient hydrogen evolution, Angew. Chem. Int. Ed. 127 (2015) 13120–13124.

[15] Y. Yang, Z. Lun, G. Xia, F. Zheng, M. He, Q. Chen, Non–precious alloy encapsulated in nitrogen–doped graphene layers derived from MOFs as an active and durable hydrogen evolution reaction catalyst, Energ. Environ. Sci. 8 (2015) 3563–3571.

[16] J. Li, Y. Tang, C. Liu, S. Li, R. Li, L. Dong, Z. Dai, J. Bao, Y. Lan, Polyoxometalate-based metal–organic framework-derived hybrid electrocatalysts for highly efficient hydrogen evolution reaction, J. Mater. Chem. A 4 (2016) 1202–1207.

[17] H. Wu, B. Xia, L. Yu, X. Yu, X. Lou, Porous molybdenum carbide nano-octahedrons synthesized via confined carburization in metal–organic frameworks for efficient hydrogen production, Nat. Commun. 6 (2015) 1–8.

[18] Y. Guo, X. Gao, C. Zhang, Y. Wu, X. Chang, T. Wang, X. Zheng, A. Du, B. Wang, J. Zheng, K. Ostrikov, X. Li, Plasma modification of a Ni based metal–organic framework for efficient hydrogen evolution, J. Mater. Chem. A 7 (2019) 8129–8135.

[19] J. Ge, D. Jiang, L. Zhang, P. Du, Embedding noble-metal-free Ni_2P cocatalyst on g–C_3N_4 for enhanced photocatalytic H_2 evolution in water under visible light, Catal. Lett. 148 (2018) 3741–3749.

[20] H. Zhao, S. Sun, P. Jiang, Z. Xu, Graphitic C_3N_4 modified by Ni_2P cocatalyst: An efficient, robust and low cost photocatalyst for visible-light-driven H_2 evolution from water, Chem. Eng. J. 315 (2017) 296–303.

[21] X. Wang, P. Clark, S. Oyama, Synthesis, characterization, and hydrotreating activity of several iron group transition metal phosphides, J. Catal. 208 (2002) 321–331.

[22] Z. Liang, X. Dong, Y. Han, J. Geng, In-situ growth of 0D/2D Ni_2P quantum dots/red phosphorus nanosheets with p-n heterojunction for efficient photocatalytic H_2 evolution under visible light, Appl. Surf. Sci. 484 (2019) 293–299.

[23] J. Bierlein, A. Sleight, Ferroelasticity in $BiVO_4$, Solid State Commun. 16 (1975) 69–70.

[24] A. Lim, S. Choh, M. Jang, Prominent ferroelastic domain walls in $BiVO_4$ crystal, J. Phys.–Condens. Mater. 7 (1995) 7309–7323.

[25] S. Tokunaga, H. Kato, A. Kudo, Selective preparation of monoclinic and tetragonal $BiVO_4$ with scheelite structure and their photocatalytic properties, Chem. Mater. 13 (2001) 4624–4628.

[26] A. Kudo, K. Omori, H. Kato, A novel aqueous process for preparation of crystal form–controlled and highly crystalline $BiVO_4$ powder from layered vanadates at room temperature and its photocatalytic and photophysical properties, J. Am. Chem. Soc. 121 (1999) 11459–11467.

[27] S. Dong, Y. Cui, Y. Wang, Y. Li, L. Hu, J. Sun, J. Sun, Designing three–dimensional acicular sheaf shaped $BiVO_4$/reduced graphene oxide composites for efficient sunlight–driven photocatalytic degradation of dye wastewater, Chem. Eng. J. 249 (2014) 102–110.

[28] J. Fu, Q. Xu, J. Low, C. Jiang, J. Yu, Ultrathin 2D/2D WO_3/g–C_3N_4 step-scheme H_2–production photocatalyst, Appl. Catal. B-Environ. 243 (2019) 556–565.

[29] Q. Xu, L. Zhang, B. Cheng, J. Fan, J. Yu, S–scheme heterojunction photocatalyst, Chem 6 (2020) 1543–1559.

[30] Y. Jiao, J. Pei, C. Yan, D. Chen, Y. Hu, G. Chen, Layered nickel metal–organic framework for high performance alkaline battery-supercapacitor hybrid devices, J. Mater. Chem. A 4 (2016) 13344–13351.

[31] X. Jiang, L. Zhang, S. Liu, Y. Zhang, Z. He, W. Li, F. Zhang, Y. Shi, W. Lü, Y. Li, et al., Ultrathin metal–organic framework: an emerging broadband nonlinear optical material for ultrafast photonics, Adv. Opt. Mater. 6 (2018), 1800561.

[32] Y. Zhang, G. Wang, W. Ma, B. Ma, Z. Jin, CdS p–n heterojunction co-boosting with Co_3O_4 and Ni–MOF-74 for photocatalytic hydrogen evolution, Dalton T. 47 (2018) 11176–11189.

[33] L. Zhang, G. Wang, X. Hao, Z. Jin, Y. Wang, MOFs–derived $Cu_3P@CoP$ p–n heterojunction for enhanced photocatalytic hydrogen evolution, Chem. Eng. J. 395 (2020), 125113.

[34] S. Zhao, J. Xu, M. Mao, L. Li, X. Li, Protonated g-C_3N_4 cooperated with Co–MOF doped with Sm to construct 2D/2D heterojunction for integrated dye-sensitized photocatalytic H_2 evolution, J. Colloid Interface Sci. 583 (2021) 435–447.

[35] S. Maiti, A. Pramanik, U. Manju, S. Mahanty, Reversible lithium storage in manganese 1,3,5–benzenetricarboxylate metal–organic framework with high capacity and rate performance, ACS Appl. Mater. Interfaces 7 (2015) 16357–16363.

[36] J. Arenas, J. Marcos, Infrared and Raman spectra of phtalic, isophtalic and terephtalic acids, Spectrochim. Acta A 36 (1980) 1075–1081.

[37] J. Yang, P. Xiong, C. Zheng, H. Qiu, M. Wei, Metal–organic frameworks: a new promising class of materials for a high performance supercapacitor electrode, J. Mater. Chem. A 2 (2014) 16640–16644.

[38] V. Maruthapandian, S. Kumaraguru, S. Mohan, V. Saraswathy, S. Muralidharan, An insight on the electrocatalytic mechanistic study of pristine Ni MOF (BTC) in alkaline medium for enhanced OER and UOR, ChemElectroChem 5 (2018) 2795–2807.

[39] X. Liu, L. Zhao, H. Lai, Y. Wei, G. Yang, S. Yin, Z. Yi, Graphene decorated MoS_2 for eosin Y–sensitized hydrogen evolution from water under visible light, RSC Adv. 7 (2017) 46738–46744.

[40] X. Liu, X. Lv, H. Lai, G. Peng, Z. Yi, J. Li, A simple Ni–based metal–organic framework as catalyst for dyesensitized photocatalytic H_2 evolution from water reduction, Photochem. Photobiol. 96 (2020) 1169–1175.

[41] Y. Zhang, Y. Liu, M. Ma, X. Ren, Z. Liu, G. Du, A. Asiri, X. Sun, A Mn–doped Ni_2P nanosheet array: an efficient and durable hydrogen evolution reaction electrocatalyst in alkaline media, Chem. Commun. 53 (2017) 11048–11051.

[42] C. Cheng, J. Shi, F. Du, S. Zong, X. Guan, Y. Zhang, M. Liu, L. Guo, Simply blending Ni nanoparticles with typical photocatalysts for efficient photocatalytic H_2 production, Catal. Sci. Technol. 9 (2019) 7016–7022.

[43] H. Tian, X. Wang, H. Li, M. Pi, D. Zhang, S. Chen, Superhydrophilic Al–doped NiP_2 nanosheets as efficient electrocatalysts for hydrogen evolution reaction, Energy Technol. 8 (2019), 1900936.

[44] Y. Li, Y. Liu, Y. Hao, X. Wang, R. Liu, F. Li, Fabrication of core-shell $BiVO_4@Fe_2O_3$ heterojunctions for realizing photocatalytic hydrogen evolution via conduction band elevation, Mater. Des. 187 (2020), 108379.

[45] X. Wu, J. Zhao, S. Guo, L. Wang, W. Shi, H. Huang, Y. Liu, Z. Kang, Carbon dot and $BiVO_4$ quantum dot composites for overall water splitting via a two–electron pathway, Nanoscale 8 (2016) 17314–17321.

[46] H. Casalongue, S. Kaya, V. Viswanathan, D. Miller, D. Friebel, H. Hansen, J. Nørskov, A. Nilsson, H. Ogasawara, Direct observation of the oxygenated species during oxygen reduction on a platinum fuel cell cathode, Nat. Commun. 4 (2013), 2041–1723.

[47] Z. Zheng, J. He, C. Dong, I. Lo, Photoelectrochemical sewage treatment by sulfite activation over an optimized $BiVO_4$ photoanode to simultaneously promote PPCPs degradation, H_2 evolution and E. coli disinfection, Chem. Eng. J. 419 (2021), 129418.

[48] X. Wang, M. Pi, D. Zhang, H. Li, J. Feng, S. Chen, J. Li, Insight into the superior electrocatalytic performance of a ternary nickel iron poly-phosphide nanosheet array: an X–ray absorption study, ACS Appl. Mater. Interfaces 11 (2019) 14059–14065.

[49] H. Gong, X. Hao, H. Li, Z. Jin, A novel materials manganese cadmium sulfide/ cobalt nitride for efficiently photocatalytic hydrogen evolution, J. Colloid Interface Sci. 585 (2021) 217–228.

[50] Y. Liu, X. Hao, H. Hu, Z. Jin, High efficiency electron transfer realized over $NiS_2/$ $MoSe_2$ S–scheme heterojunction in photocatalytic hydrogen evolution, Acta Phys. Chim. Sin. 37 (2021), 2008030.

[51] J. Li, X. Wu, S. Liu, Fluorinated TiO_2 hollow photocatalysts for photocatalytic applications, Acta Phys. Chim. Sin. 37 (2021), 2009038.

[52] H. Li, G. Wang, H. Gong, Z. Jin, Hollow nanorods and amorphous Co_9S_8 quantum dots construct S–Scheme heterojunction for efficient hydrogen evolution, J. Phys. Chem. C 125 (2021) 648–659.

[53] J. Guo, Y. Liang, L. Liu, J. Hu, H. Wang, W. An, W. Cui, Noble-metal-free CdS/ Ni–MOF composites with highly efficient charge separation for photocatalytic H_2 evolution, Appl. Surf. Sci. 522 (2020), 146356.

[54] M. Li, J. Li, Z. Jin, 0D/2D spatial structure of $Cd_xZn_{1-x}S$/Ni-MOF-74 for efficient photocatalytic hydrogen evolution, Dalton T. 49 (2020) 5143–5156.

[55] W. Luo, X. Chen, Z. Wei, D. Liu, W. Yao, Y. Zhu, Three–dimensional network structure assembled by g–C_3N_4 nanorods for improving visible–light photocatalytic performance, Appl. Catal. B-Environ. 255 (2019), 117761.

[56] P. Niu, L. Zhang, G. Liu, H. Cheng, Graphene–like carbon nitride nanosheets for improved photocatalytic activities, Adv. Funct. Mater. 22 (2012) 4763–4770.

[57] P. Yang, H. Ou, Y. Fang, X. Wang, A facile steam reforming strategy to delaminate layered carbon nitride semiconductors for photoredox catalysis, Angew. Chem. Int. Ed. 56 (2017) 3992–3996.

[58] Z. Jin, Y. Li, X. Hao, Ni, Co-based selenide anchored g-C$_3$N$_4$ for boosting photocatalytic hydrogen evolution, Acta Phys. Chim. Sin. 37 (2021), 1912033.

[59] Z. Jin, Y. Liu, X. Hao, Self-assembly of zinc cadmium sulfide nanorods into nanoflowers with enhanced photocatalytic hydrogen production activity, J. Colloid Interface Sci. 567 (2020) 357–368.

[60] X. Li, J. Yu, J. Low, Y. Fang, J. Xiao, X. Chen, Engineering heterogeneous semiconductors for solar water splitting, J. Mater. Chem. A 3 (2015) 2485–2534.

[61] C. Regmi, Y. Kshetri, D. Dhakal, J. Sohng, F. Rosei, S. Lee, Insight into phosphate doped BiVO$_4$ heterostructure for multifunctional photocatalytic performances: a combined experimental and DFT study, Appl. Surf. Sci. 466 (2019) 787–800.

[62] S. Shi, Z. Li, Y. Sun, B. Wang, Q. Liu, Y. Hou, S. Huang, J. Huang, Y. Zhao, A covalent heterostructure of monodisperse Ni$_2$P immobilized on N, P–codoped carbon nanosheets for high performance sodium/lithium storage, Nano Energy 48 (2018) 510–517.

[63] C. Stampfl, C. Walle, Density-functional calculations for III–V nitrides using the local–density approximation and the generalized gradient approximation, Phys. Rev. B 59 (1999) 5521–5535.

[64] H. He, J. Cao, M. Guo, H. Lin, J. Zhang, Y. Chen, S. Chen, Distinctive ternary CdS/Ni$_2$P/g–C$_3$N$_4$ composite for overall water splitting: Ni$_2$P accelerating separation of photocarriers, Appl. Catal. B-Environ. 249 (2019) 246–256.

[65] K. Ordon, A. Kassiba, M. Janusik, Electronic, optical and vibrational features of BiVO$_4$ nanostructures investigated by first principles calculations, RSC Adv. 6 (2016) 110695–110705.

[66] Y. Li, Z. Jin, L. Zhang, K. Fan, Controllable design of Zn–Ni–P on g–C$_3$N$_4$ for efficient photocatalytic hydrogen production, Chin. J. Catal. 40 (2019) 390–402.

[67] J. Wang, G. Wang, B. Cheng, J. Yu, J. Fan, Sulfur–doped g–C$_3$N$_4$/TiO$_2$ S–scheme heterojunction photocatalyst for congo red photodegradation, Chin. J. Catal. 42 (2021) 56–68.